Ultrasound Beam Simulations in Inhomogeneous Tissue Geometries Using the Hybrid Angular Spectrum Method

Urvi Vyas and Douglas Christensen

***Abstract*—The angular spectrum method is a fast, accurate and computationally efficient method for modeling wave propagation. However, the traditional angular spectrum method assumes that the region of propagation has homogenous properties. In this paper, the angular spectrum method is extended to calculate ultrasound wave propagation in inhomogeneous tissue geometries, important for clinical efficacy, patient safety, and treatment reliability in MR-guided focused ultrasound surgery. The inhomogeneous tissue region to be modeled is segmented into voxels, each voxel having a unique speed of sound, attenuation coefficient, and density. The pressure pattern in the 3-D model is calculated by alternating between the space domain and the spatial-frequency domain for each plane of voxels in the model. The new technique was compared with the finite-difference time-domain technique for a model containing attenuation, refraction, and reflection and for a segmented human breast model; although yielding essentially the same pattern, it results in a reduction in calculation times of at least two orders of magnitude.**

I. Introduction

Magnetic resonance-guided focused ultrasound surgery (MRgFUS) has received a great deal of attention in recent years because of its non-invasive nature, localized tissue effects, and temperature feedback. For safe, effective, and efficient treatment, controlling the energy deposited by the ultrasound beam is imperative. Refraction, reflection, and particularly absorption of the ultrasound beam in inhomogeneous tissue geometries of the human body determine the specific power deposition pattern. Fast and accurate prediction of this pattern will help in control and guidance of the MRgFUS treatment.

The Rayleigh-Sommerfeld integral [1] is a popular technique to calculate pressure fields from rectangular [2], circular [3], triangular, and irregular multisided polygon-shaped sources [4], assuming a homogeneous, isotropic medium for propagation. It has also been extended to layered media (composed of homogeneous layers, each layer with different properties) [5]. The finite-difference time-domain (FDTD) approach, which employs numerical approximations of the spatial and temporal partial derivatives about each node of a grid, has been implemented to model wave propagation in inhomogeneous media [6]. Although it is a powerful technique, limits on the maximum size of the voxels and time steps that can be used lead to long computation times. The Fourier split-step technique has been used for modeling wave propagation in underwater acoustics [7] and seismic migration [8]. The technique calculates the effect of a varying velocity in the medium by alternating back and forth between the frequency-wavenumber and frequency-space domains. The technique handles slowly changing values of velocity without taking into account changes caused by attenuation.

For rapid beam simulations, the angular spectrum method has been used extensively [9]–[11]. This approach assumes linear propagation and steady-state conditions. The numerical implementation and parameter selection for the angular spectrum method have been discussed in the literature [12]–[14] and the method has been shown to be fast and accurate for homogeneous tissue. The method has also been extended to model wave propagation in layers of homogeneous media [15]–[16].

The hybrid angular spectrum (HAS) technique [17] presented here can model linear wave propagation in inhomogeneous media and the irregular geometries of the human body. It is an extension of the traditional angular spectrum method that accounts not only for layers of homogenous tissue but also within-layer differences in tissue properties.

II. Traditional Angular Spectrum Method

Fig. 1 shows the traditional angular spectrum method, which assumes that the tissue between the initial and final pressure planes has homogeneous acoustic properties. Using the fast Fourier transform (FFT) algorithm, the pressure pattern on the initial plane $p'(x, y, 0)$ is encoded into a spectrum $A'(\alpha/\lambda, \beta/\lambda; 0)$ of traveling plane waves in the spatial-frequency domain [11]. These waves travel at different angles that depend on their spatial frequencies f_x and f_y according to direction cosines $\alpha = \lambda f_x$ and $\beta = \lambda f_y$ (with the zero spatial-frequency component propagating perpendicular to the plane). Propagation of the waves to the next plane is then calculated in the spatial-frequency domain by multiplying the initial spectrum by the propagation transfer function

$$H(\alpha, \beta) = e^{j(2\pi/\lambda)\sqrt{1-\alpha^2-\beta^2}\Delta z} \tag{1}$$

to account for the longitudinal path length Δz between the two planes. An inverse fast Fourier transform (IFFT)

Manuscript received August 9, 2011; accepted February 10, 2012.

The authors are with the Department of Bioengineering, University of Utah, Salt Lake City, UT (e-mail: urvivyas@gmail.com).

D. Christensen is also with the Department of Electrical and Computer Engineering, University of Utah, Salt Lake City, UT.

DOI http://dx.doi.org/10.1109/TUFFC.2012.2300

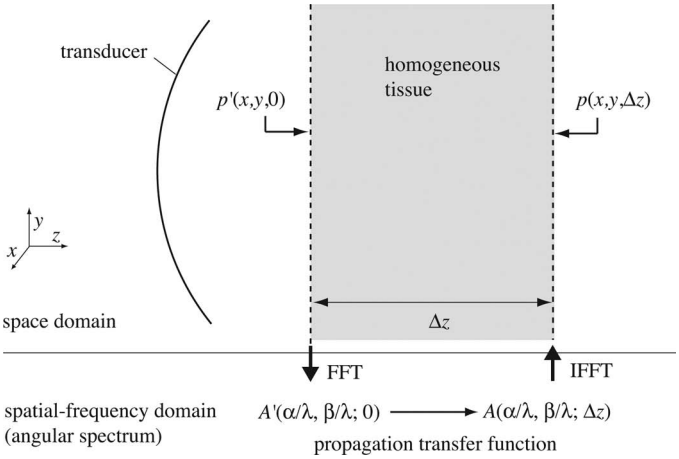

Fig. 1. Traditional angular spectrum method with the angular spectrum expressed in terms of direction cosines $\alpha = \lambda f_x$ and $\beta = \lambda f_y$, where f_x and f_y are spatial frequencies.

of the angular spectrum of the propagated waves gives the pressure pattern $p(x, y, \Delta z)$ at the final plane in the space domain. The use of FFT and IFFT makes this technique very fast.

III. Hybrid Angular Spectrum Method

In the hybrid angular spectrum (HAS) method, the 3-D inhomogeneous tissue geometry is divided into rectangular voxels (i.e., rectangular cuboids), each voxel associated with a unique tissue type having its own speed of sound, attenuation coefficient, and density, as shown in Fig. 2(a). For MRgFUS, the model is often obtained by segmenting a magnetic resonance image of the object and selecting the nominal acoustic parameters for the tissue types from literature values. The pressure pattern in the model is calculated sequentially, plane-by-plane, through successive transverse planes of voxels progressing in the direction of propagation away from the transducer. Within each plane, the acoustic properties may change between voxels in the x- and y-directions, but within each individual voxel, the tissue properties are considered constant. The calculation sequence alternates back-and-forth between the space domain and the spatial-frequency domain for each plane of voxels. Wave propagation through each plane is therefore calculated in two steps, one in the space domain and one in the spatial-frequency domain, as described shortly. The method simulates the propagation of linear longitudinal pressure waves at steady state.

The angular spectrum technique allows the decomposition of the pressure wave into a set of tilted plane waves. The transmission of one of these plane-wave components (at one given angle in the angular spectrum) of the pressure pattern $p_{n-1}(x, y)$ through the nth plane can be described in the space domain by

$$p_n(x, y) = p_{n-1}(x, y) \cdot t_n(x, y), \tag{2}$$

where $t_n(x, y)$ is a transmission function given by

$$t_n(x, y) = e^{jb_n(x,y)r' - a_n(x,y)r}, \tag{3}$$

with the first term in the exponent representing phase change and the second term representing attenuation as functions of x and y. Here, $b_n(x, y) = 2\pi/\lambda_n = 2\pi f/c_n(x, y)$ is the propagation constant at various x-y voxel locations [found from the specific speed of sound $c_n(x, y)$ and temporal frequency f], $a_n(x, y)$ is the pressure attenuation coefficient of the individual voxels, r' is the perpendicular distance measured between two parallel wavefronts of the tilted plane wave component, and r is the oblique distance across the layer at the angle of the plane wave, as shown in Fig. 2(a). The two distances r' and r are used to take into account different effects as the wave component travels through the layer: r' is the effective path length between two tilted wavefronts that intercept the origins of the two planes forming the layer and is used in the phase

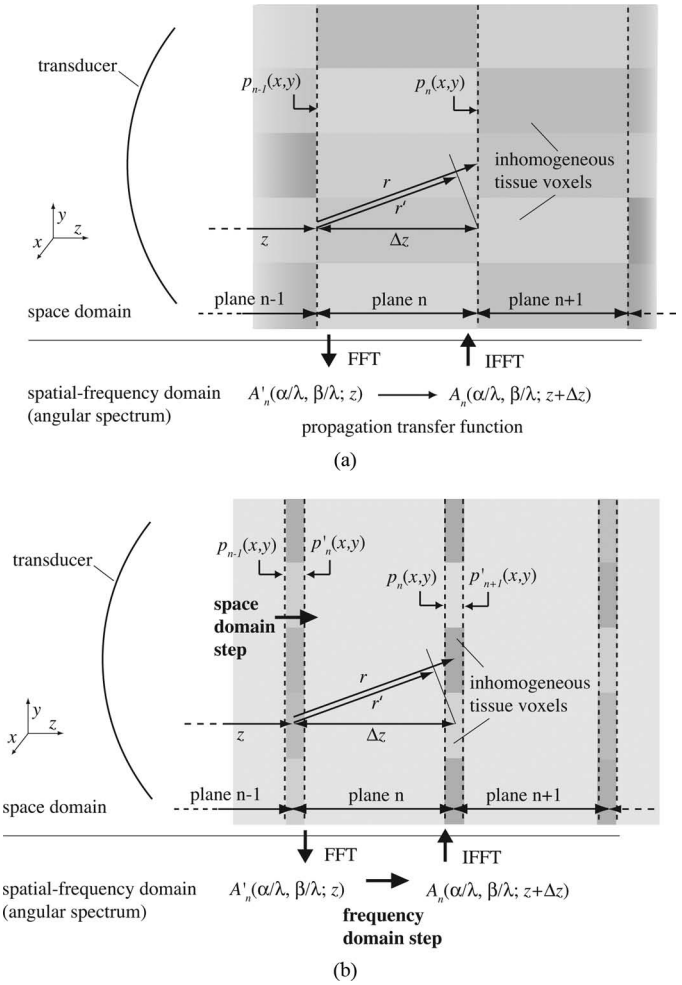

Fig. 2. Hybrid angular spectrum method. (a) The inhomogeneous model is divided into rectangular voxels and calculations are done plane-by-plane in the propagation direction, first in the space domain, then in the spatial-frequency domain; in 3-D, r and r' are usually tilted out of the plane of the figure. (b) To help conceptualize the two-step process at each plane of voxels, the variations in the voxels' acoustic properties from the planar average are collapsed into a thin layer through which the beam first travels in the space domain, then is propagated to the next plane by an average transfer function in the frequency domain.

term that expresses the phase change encountered by the plane wave component, whereas the distance r is the entire propagation path of the wave component inside the layer and is used in the term that models attenuation of that component inside the layer.

To facilitate the two-step process, the phase change $b_n(x,y)r'$ across each plane of voxels is divided into two parts, an average phase shift $b_n'r'$ calculated for that plane, and the difference $\Delta b_n(x,y)r'$ from the average phase shift for the various voxels inside the plane. Thus the transmission function becomes

$$t_n(x,y) = e^{jb_n'r'}e^{j\Delta b_n(x,y)r'}e^{-a_n(x,y)r}. \tag{4}$$

In determining the x-y-averaged propagation constant b_n' for each plane, the averaging is weighted by the magnitude of the pressure spatial pattern (that is, weighted according to where the preponderance of the beam is estimated to be in that plane). Thus,

$$\begin{aligned} b_n' &= \frac{\int |p_{n-1}(x,y)| b_n(x,y) \mathrm{d}x\mathrm{d}y}{\int |p_{n-1}(x,y)| \mathrm{d}x\mathrm{d}y} \\ &= \frac{2\pi \int |p_{n-1}(x,y)| (f/c_n(x,y)) \mathrm{d}x\mathrm{d}y}{\int |p_{n-1}(x,y)| \mathrm{d}x\mathrm{d}y}, \end{aligned} \tag{5}$$

and

$$\Delta b_n(x,y) = \frac{2\pi f}{c_n(x,y)} - b_n'. \tag{6}$$

The two-step process then proceeds as follows: propagation changes due to the term $e^{j\Delta b_n(x,y)r'}e^{-a_n(x,y)r}$ are calculated in the space domain, whereas changes due to term $e^{jb_n'r'}$ are calculated in the spatial-frequency domain. This may be most easily visualized conceptually by considering that the x-y-varying portions of the plane's voxels (i.e., the phase shift difference and attenuation) are collapsed into a thin layer at the front of each plane through which the pressure pattern is transmitted in the space domain (still maintaining the values of r and r'), after which the pattern is propagated to the next plane in the spatial-frequency domain. This concept is illustrated in Fig. 2(b) and described next.

A. Space Domain Step

If $p_{n-1}(x,y)$ is the pressure at the entrance to plane n, then the pressure $p_n'(x,y)$ after passing through the thin layer in the space domain is

$$p_n'(x,y) = p_{n-1}(x,y)e^{j\Delta b_n(x,y)r'}e^{-a_n(x,y)r}. \tag{7}$$

As shown in Fig. 2(a), r and r' will vary depending on the angles of the various plane-wave components of the angular spectrum. To account for this variation, the values of r and r', which are constants in (7) for a given plane, are calculated with a weighting factor based on the magnitude of the angular spectrum at the entrance of this plane.

B. Spatial-Frequency Domain Step

The resulting pressure pattern $p_n'(x,y)$ is then Fourier transformed (denoted by the symbol $\mathfrak{F}\{\ldots\}$) to obtain the angular spectrum $A_n'(\alpha/\lambda, \beta/\lambda; z)$ before propagation across the plane:

$$A_n'\left(\frac{\alpha}{\lambda}, \frac{\beta}{\lambda}; z\right) = \mathfrak{F}\{p_n'(x,y)\}. \tag{8}$$

Propagation across the plane is accomplished in the spatial-frequency domain using the propagation transfer function incorporating the average propagation constant b_n':

$$A_n\left(\frac{\alpha}{\lambda}, \frac{\beta}{\lambda}; z+\Delta z\right) = A_n'\left(\frac{\alpha}{\lambda}, \frac{\beta}{\lambda}; z\right)e^{jb_n'\sqrt{1-\alpha^2-\beta^2}\Delta z}, \tag{9}$$

where r' (now a variable) has been replaced with an equivalent geometric expression involving direction cosines α and β, effectively implementing the propagation transfer function of (1).

The pressure $p_n(x,y)$ at the entrance to the next plane of voxels in the space domain is found from an inverse Fourier transform:

$$p_n(x,y) = \mathfrak{F}^{-1}\left\{A_n\left(\frac{\alpha}{\lambda}, \frac{\beta}{\lambda}; z+\Delta z\right)\right\}. \tag{10}$$

This sequence is repeated for each subsequent plane of voxels to obtain the forward-propagating pressure pattern in the 3-D model.

In summary, the pressure wave is propagated through each plane by dividing the acoustic properties of the plane into two parts: the average phase shift for the plane and the difference from the average phase shift for each voxel in the plane. In the space-domain step (7), the effect of the attenuation and the difference from average phase shift of each voxel in the plane is calculated and the incoming pressure pattern is multiplied by these two effects. In the spatial-frequency domain step (9), the effect of the average phase shift for the entire plane is incorporated in the propagation transfer function. Propagation takes place plane-by-plane through the entire 3-D model.

C. First-Order Reflections

First-order reflections in the model are calculated in the space domain using the reflection coefficient at each interface. The pressure reflection coefficient [18] at an interface is determined by the impedance mismatch between voxel pairs:

$$R_n(x,y) = \frac{Z_n(x,y) - Z_{n-1}(x,y)}{Z_n(x,y) + Z_{n-1}(x,y)}, \tag{11}$$

where $Z_n(x, y) = \rho_n(x, y)c_n(x, y)$ is the acoustic impedance and $\rho_n(x, y)$ is the density of the voxels. At each interface, the corresponding reflection coefficient is used to calculate the part of the forward pressure that is reflected (and temporarily stored), the rest being transmitted. First, the full forward wave is assembled plane-by-plane, as described in the previous section, using only the transmitted pressure component at each interface. Following this, the reflected wave is initiated with zero magnitude at the rear model boundary and propagated plane-by-plane in the backward direction (opposite to the direction of forward propagation), with the stored reflected pressure patterns at each interface added to this backward propagating wave. The backward propagation uses the same alternation between the space domain and the spatial-frequency domain as the forward propagating wave. Finally the forward and the backward propagating waves are added together in complex notation to give the final pressure pattern for the 3-D inhomogeneous model.

IV. Numerical Implementation Details

The effects of sampling in the space domain and spatial-frequency domain in the traditional angular spectrum method have been described previously [19], [20]. The general angular spectrum approach is independent of the particular algorithms used to obtain the Fourier transforms, but because we use the popular Matlab functions FFT and IFFT (The MathWorks, Natick, MA), the sampling interval and extent of the spatial-frequency domain are linked to the sampling interval and extent of the space domain.

A. Size of Voxels

The size of the voxels in the space domain (Δx and Δy) sets the overall size of the spatial-frequency domain; for example, $f_{x,\max} = 1/(2\Delta x)$, a consequence of the FFT algorithm. The maximum size of the voxels in the space domain, therefore, is limited by the highest desired spatial-frequency content in the beam's features. To eliminate aliasing resulting from under-sampling in the space domain, the sampling frequency in the space domain should be at least as high as the Nyquist criterion ($1/\Delta x \geq$ twice the highest desired spatial frequency). If needed, the highest spatial-frequency components of the angular spectrum can be restricted using ray theory truncation [10] or angular restriction techniques [19]. (Frequencies higher than $1/\lambda$ are effectively non-propagating because they are evanescent.) Smaller voxels result in longer calculation times but produce smoother beam patterns; they also reduce the stair-stepping effect at oblique interfaces that results from segmenting the model into rectangular voxels. For our application, which uses this simulation software to guide MRgFUS, the size of the voxels is normally set equal to the resolution of the magnetic resonance images, usually on the order of 1-mm isotropic resolution.

B. Size of the Space Domain

The overall extent of the space domain (L_x and L_y) should be at least as large as the model itself, but may need to be increased due to consideration of wraparound errors, a consequence of having a sampling interval Δf_x in the frequency domain that is too large. Because $\Delta f_x = 1/L_x$, wraparound errors, which are due to under-sampling in the frequency domain, as explained in Section VI, can be eliminated by increasing the overall size of the space domain by zero padding.

C. Number of Voxels

The number of voxels in the model is then determined by the size of the voxels (Δx and Δy) and the overall size of the space domain (L_x and L_y). To avoid the half-sample phase-shift error [21] the number of voxels in the model in the x- and y-directions should be odd.

D. Pressure Pattern on the Initial Plane

One of the requirements for both the angular spectrum method and our implementation of the HAS technique is that the initial pressure pattern must be specified on a plane. When using curved transducers with either technique, a separate beam simulation method is required to calculate the pressure pattern from the curved transducer surface to the initial plane of the inhomogeneous model. A homogeneous beam propagation technique, such as the Rayleigh-Sommerfeld integral, can be used to calculate this initial pressure because the space between the transducer and the front plane of the model in almost all simulations is comprised of water (or a similar homogeneous coupling liquid).

To keep the overall calculation time of our simulation short we have developed a faster method to calculate the initial pressure field from a curved phased-array transducer using pre-calculated Rayleigh-Sommerfeld patterns, called the element response function array (ERFA) technique [17]. The response of each element of the phased array (normalized by assuming zero phase and unit amplitude) is pre-calculated and stored as one page in the ERFA. During run time, each page is multiplied by the appropriate element phase and amplitude (to account for electronic steering and an arbitrary excitation pattern) and all pages are summed in complex notation (a fast calculation) to obtain the resulting pressure pattern at the initial plane of the inhomogeneous model. This reduces the run-time calculation time by three orders of magnitude compared with a full Rayleigh-Sommerfeld calculation at run time.

V. Results

For validation purposes, the HAS technique was first compared with a FDTD simulation [6] using a high-reso-

TABLE I. ULTRASOUND PROPERTIES USED IN VALIDATION MODEL.

	Speed of sound (m/s)	Attenuation (Np/(cm·MHz))	Density (kg/m^3)
Wedge	2000	0	600
Cylinder	1500	2.0	1000
Water	1500	0	1000

lution three-medium inhomogeneous 3-D wedge/cylinder model configured to exhibit reflection, refraction, and attenuation. The validation model contained 141 × 141 × 121 voxels with 0.15-mm isotropic resolution, as shown in Fig. 3, with acoustic properties (Table I) purposely chosen to emphasize the effects on beam propagation. Both numerical techniques assumed a solid (i.e., single-element spherically focused) 1.5-MHz transducer with an outer diameter (aperture diameter) of 10 cm and a geometric focus (radius of curvature) of 18 cm. The transducer was located 17 cm away from the initial model plane; the pressure at the initial plane was calculated using the Rayleigh-Sommerfeld integral. The numerical simulations for this model were done on a 2.0-GHz dual-core Windows (Microsoft Corp., Redmond, WA) laptop with 3 GB of RAM using Matlab version 7.10.

To quantify the comparison between the two methods, the normalized root-mean-square (nrms) difference between the two pressure patterns was calculated according to

$$\Delta_{\text{nrms}} = \sqrt{\frac{\sum_{i=1}^{N} |p_{\text{HAS}}(i) - p_{\text{FDTD}}(i)|^2}{N}}, \qquad (12)$$

where $p_{\text{HAS}}(i)$ and $p_{\text{FDTD}}(i)$ are the normalized pressures calculated using the HAS technique and the FDTD technique, respectively, at each voxel i in the 3-D volume. This metric accounts for both magnitude and phase differences between the two methods. Each beam pattern was normalized to the highest pressure found in their respective 3-D volumes (i.e., at the beam focus).

Longitudinal slices through the center of focus of the magnitude of the calculated pressure using the HAS and FDTD methods are shown in Figs. 4(a) and 4(b), respectively. There was a significant difference in the calculation times for each method (not including the time for the initial Rayleigh-Sommerfeld calculation): the HAS technique took 9.5 s for the full 3-D simulation, whereas the FDTD technique took 67 min. (The FDTD pressure pattern was actually calculated for a model 25% longer in the direction of propagation than shown in Fig. 4(b), then truncated to avoid displaying reflections from the far boundary of the model, which did not employ radiating boundary conditions; the HAS technique inherently incorporates effective radiating boundary conditions at the far model boundary.) The root-mean-square difference between the two simulated patterns was found to be $\Delta_{\text{nrms}} = 0.013$ over the 3-D model.

Further, to illustrate the technique in a clinically relevant situation, we chose an inhomogeneous model derived from a segmented magnetic resonance image of a patient with breast cancer. The 3-D breast model was segmented by hand into three tissue types—breast fat, fibro-glandular tissue, and breast cancer—and divided into 301 × 301 × 300 voxels with 0.15-mm isotropic resolution ($\lambda/10$ at 1 MHz). One longitudinal slice view is shown in Fig. 5. The ultrasound properties for the tissue types, listed in Table II, were estimated using values from [22] and [23]. A 256-element, 1-MHz, spherically curved, 14.5-cm outer diameter phased-array transducer with a geometric focus of 13 cm and located 11 cm away from the initial plane of the breast model was assumed. The pressure pattern on the initial plane was calculated using the ERFA method, described previously. First-order reflections were included for all results. These numerical simulations were done on a 2.67-GHz i7-core (Intel Corp., Santa Clara, CA) Windows desktop with 12 GB of RAM using Matlab version 7.10.

Figs. 6(a) and 6(b) are longitudinal slices through the beam's focal center showing the magnitude of the pressure calculated using the HAS technique and the FDTD technique, respectively, when the beam was electronically steered away from its geometric focus by 10.6, 0, and 2.6 mm in x, y, and z directions. This particular steering direction was chosen such that the focus was located in a

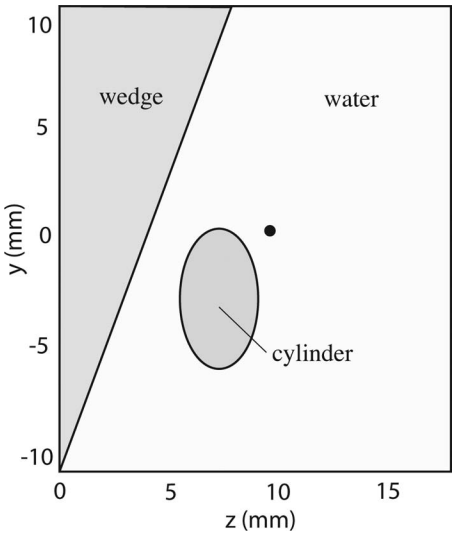

Fig. 3. Longitudinal slice view of the 3-D model for comparing the results of the hybrid angular spectrum technique with the finite-difference time-domain technique. The acoustic properties of the three features (given in Table I) were chosen to emphasize refraction, reflection, and attenuation. The wedge and cylinder extend through the entire width of the model in the x-direction. The model has 141 × 141 × 121 voxels with 0.15-mm isotropic resolution. A solid (i.e., single-element spherically focused) 1.5-MHz, 10-cm aperture diameter transducer (18-cm radius of curvature) is located 17 cm to the left of the figure with its focus at the dot.

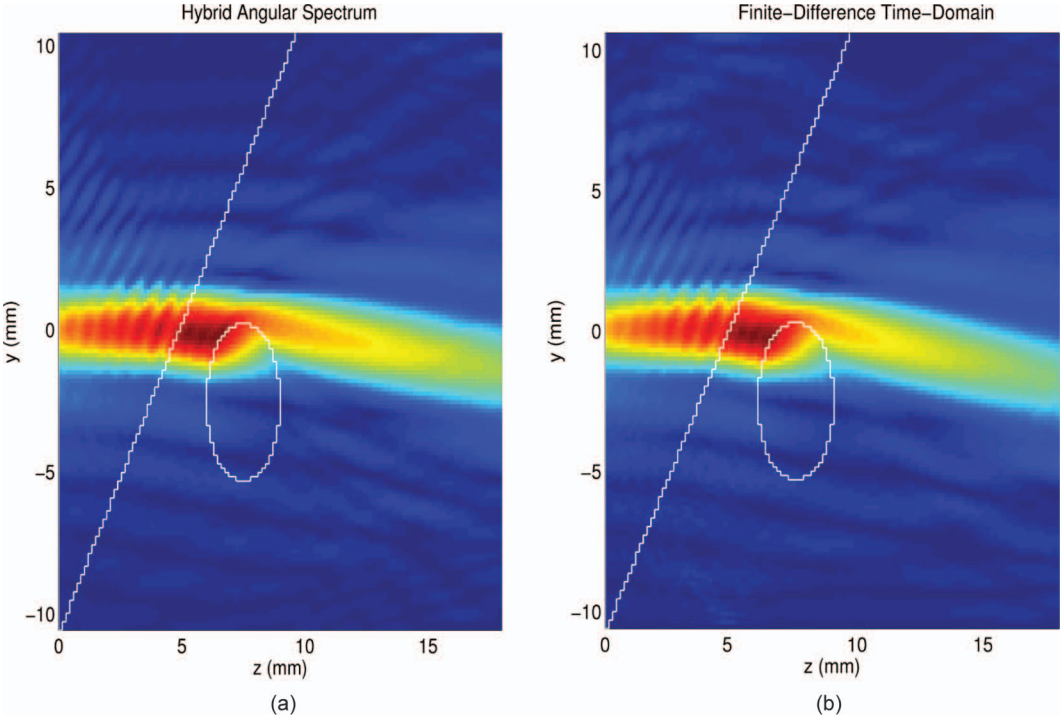

Fig. 4. Longitudinal slice views of the magnitude of the pressure pattern through the focus of the model shown in Fig. 3 using (a) the hybrid angular spectrum method, and (b) the finite-difference time-domain method. Both patterns are normalized to the highest pressure found in their respective 3-D volumes.

region of breast cancer. The full 3-D calculation time (not including the Rayleigh-Sommerfeld calculations to the initial plane) using the HAS technique for this model was approximately 46 s, whereas the FDTD technique took 467 min. The normalized rms difference between the two patterns calculated over the entire 3-D model was $\Delta_{\text{nrms}} = 0.028$.

VI. Discussion

The traditional angular spectrum technique and, hence, the HAS approach are both plane-to-plane propagation techniques; a prerequisite for these methods is that the initial pressure pattern must be calculated on the model's first plane using a homogeneous beam propagation technique, such as the Rayleigh-Sommerfeld integral or the ERFA pre-calculation technique used in this paper, to account for propagation from the curved transducer to the first plane. The ERFA method has proven to be fast and can handle changing electronic beam-steering conditions at run time.

The HAS technique does not require the user to explicitly set any boundary conditions; the implicit boundary conditions for the model are: 1) a radiating boundary at the model's rear face normal to the axis of propagation, because no reflections are implemented there; and 2) totally reflecting boundaries at the model's edges parallel to the axis of propagation, a consequence of spatial wraparound [10]. Wraparound can be explained as follows: Because of the discrete frequency domain sampling employed in the HAS technique (for example at intervals Δf_x in the f_x-direction), the effective space domain pattern can be regarded as an infinitely large patchwork made up of repeating source planes at repeat distances equal to, in this example, $L_x = 1/\Delta f_x$ in the x-direction. As the plane waves of the angular spectrum propagate deeper into the model at various angles, high-angle (high-frequency) waves from adjacent source planes can enter the propagating space

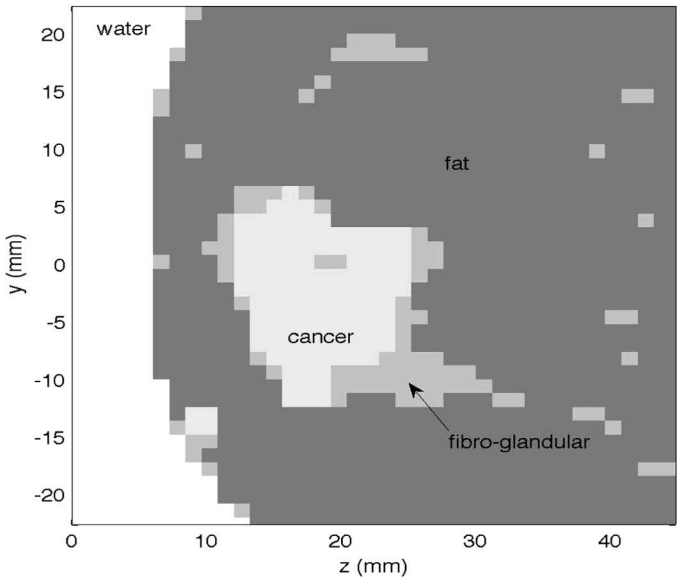

Fig. 5. Longitudinal slice view of 3-D breast model segmented into three tissue types, as labeled. A 256-element, 1-MHz phased-array transducer with a 13-cm geometric focus is located 11 cm to the left of the figure.

TABLE II. ULTRASOUND TISSUE PROPERTIES USED IN BREAST MODEL.

	Speed of sound (m/s)	Attenuation (Np/(cm·MHz))	Density (kg/m^3)
Water	1500	0	1000
Breast cancer	1560	0.133	1064
Fibro-glandular tissue	1480	0.091	937
Breast fat	1480	0.086	937

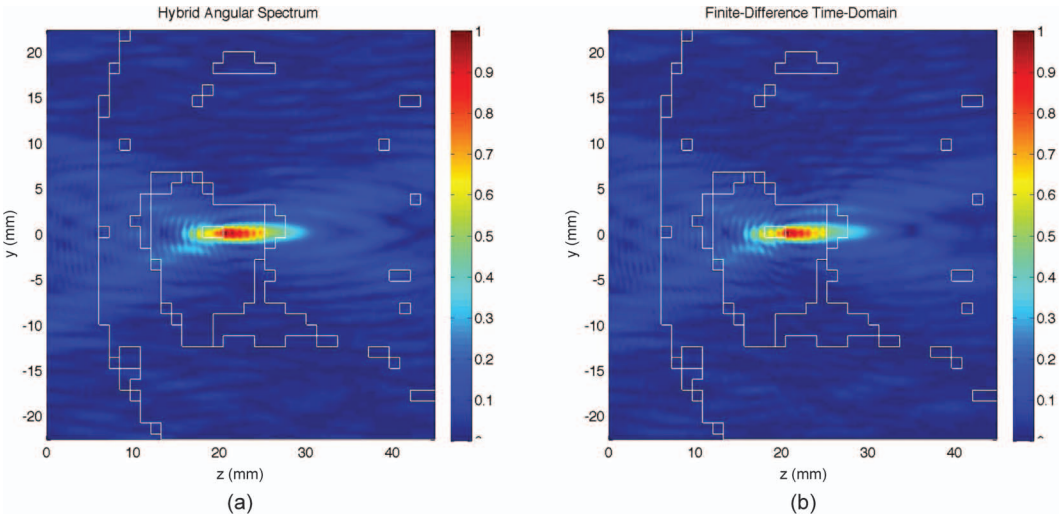

Fig. 6. Longitudinal slice views of the magnitude of the calculated pressure pattern through the focus in the segmented breast model of Fig. 5 using (a) the hybrid angular spectrum method, and (b) the finite-difference time-domain method. The beam is electronically steered away from the geometric focus by 10.6, 0, and 2.6 mm in the x, y, and z-directions.

of the central volume. This results in wraparound in the space domain as the waves propagate deeper into the model, and is equivalent to total reflecting boundary conditions at the model edges parallel to the axis of propagation. For the examples presented in this paper, the beams were focused tightly enough near the center of the models that any reflections from lateral walls were negligible.

Fig. 4 displays the comparison between the pressure patterns calculated using the HAS and the FDTD techniques for the model of Fig. 3. Because of the impedance mismatch at the wedge–water interface, reflections and a partial standing wave pattern can be seen in front of the oblique wedge interface in both patterns. The angle of beam refraction resulting from the tilted wedge–water interface is essentially equal for both techniques. A high-pressure region can be seen just beyond the wedge in both patterns, due mainly to focusing of the beam, but attenuation by the highly attenuating cylinder significantly reduces the intensity in the beam propagating through and past the cylinder. The two techniques yielded effectively the same pressure patterns: the nrms difference in pressures over the 3-D model was only 1.3%.

Fig. 6 shows that the HAS technique is able to calculate pressure patterns for an inhomogeneous 3-D model, including accounting for electronic steering of the ultrasound beam. It correctly predicts the location of the steered focus, and simulates details of the first-order reflections from the rear surface of the breast cancer region when the phased-array transducer is electronically steered toward that location, as seen in Figs. 6(a) and 6(b). The nrms difference between the calculated pressure patterns using the HAS and FDTD techniques over the 3-D model was 2.8%.

VII. CONCLUSIONS

The HAS technique calculates the complex pressure pattern in an inhomogeneous 3-D model. It assumes steady-state and linear propagation conditions. The technique is rapid, resulting in a decrease in calculation time of more than two orders of magnitude compared with the FDTD technique, while giving essentially the same pressure pattern.

REFERENCES

[1] J. W. S. Rayleigh, *The Theory of Sound*, vol. 1, New York, NY: Dover, 1945.

[2] K. B. Ocheltree and L. A. Frizzel, "Sound field calculation for rectangular sources," *IEEE Trans. Ultrason. Ferroelectr. Freq. Control*, vol. 36, no. 2, pp. 242–248, 1989.

[3] C. Lee and P. J. Benkeser, "Computationally efficient sound field calculations for a circular array transducer," *IEEE Trans. Ultrason. Ferroelectr. Freq. Control*, vol. 39, no. 1, pp. 43–47, 1992.

[4] J. A. Jensen and N. B. Svendsen, "Calculation of pressure fields from arbitrarily shaped, apodized, and excited ultrasound transducers," *IEEE Trans. Ultrason. Ferroelectr. Freq. Control*, vol. 39, no. 2, pp. 262–267, 1992.
[5] X. Fan and K. Hynynen, "The effects of wave reflection and refraction at soft tissue interfaces during ultrasound hyperthermia treatments," *J. Acoust. Soc. Am.*, vol. 91, no. 3, pp. 1727–1736, 1992.
[6] M. Cizek and J. Rozman, "Acoustic wave equation simulation using FDTD," in *17th Int. Conf. Radioelektronika*, 2007, pp. 1–4.
[7] P. L. Stoffa, J. T. Fokkema, R. M. D. Freire, and W. P. Kessinger, "Split-step Fourier migration," *Geophysics*, vol. 55, no. 4, pp. 410–414, 1990.
[8] L.-J. Huang and M. C. Fehler, "Accuracy analysis of the split-step Fourier propagator; Implications for seismic modeling and migration," *Bull. Seismol. Soc. Am.*, vol. 88, no. 1, pp. 18–29, 1998.
[9] J. A. Ratcliffe, "Some aspects of diffraction theory and their application to the ionosphere," *Rep. Prog. Phys.*, vol. 19, pp. 188–267, 1956.
[10] P. T. Christopher and K. J. Parker, "New approaches to the linear propagation of acoustic fields," *J. Acoust. Soc. Am.*, vol. 90, no. 1, pp. 507–521, 1991.
[11] J. W. Goodman, *Introduction to Fourier Optics*, 3rd ed., Greenwood Village, CO: Roberts and Co., 2004.
[12] P. Wu, R. Kazys, and T. Stepinski, "Optimal selection of parameters for the angular spectrum approach to numerically evaluate acoustic fields," *J. Acoust. Soc. Am.*, vol. 101, no. 1, pp. 125–134, 1997.
[13] P. Wu and T. Stepinski, "Extension of the angular spectrum approach to curved radiators," *J. Acoust. Soc. Am.*, vol. 105, no. 5, pp. 2618–2627, 1999.
[14] X. Zeng and R. J. McGough, "Optimal simulations of ultrasonic fields produced by large thermal therapy arrays using the angular spectrum approach," *J. Acoust. Soc. Am.*, vol. 125, no. 5, pp. 2967–2977, 2009.
[15] C. J. Vecchio, M. E. Schafer, and P. A. Lewin, "Prediction of ultrasonic field propagation through layered media using the extended angular spectrum method," *Ultrasound Med. Biol.*, vol. 20, no. 7, pp. 611–622, 1994.
[16] D. Belgroune, J. F. Belleval, and H. Djelouah, "Modeling of the ultrasonic field by the angular spectrum method in presence of interface," *Ultrasonics*, vol. 40, pp. 297–302, 2002.
[17] U. Vyas and D. A. Christensen, "Ultrasound beam propagation using the hybrid angular spectrum method," in *30th Annu. Int. Conf. IEEE Engineering in Medicine and Biology Society*, 2008, pp. 2526–2529.
[18] D. A. Christensen, *Ultrasonic Bioinstrumentation*. New York, NY: Wiley, 1988.
[19] D. P. Orofino and P. C. Pedersen, "Efficient angular spectrum decomposition of acoustic sources. I. Theory," *IEEE Trans. Ultrason. Ferroelectr. Freq. Control*, vol. 40, no. 3, pp. 238–249, 1993.
[20] P. Wu, R. Kazys, and S. Tadeusz, "Analysis of the numerically implemented angular spectrum approach based on the evaluation of two dimensional acoustic fields. Part II. Characteristics as a function of angular range," *J. Acoust. Soc. Am.*, vol. 99, no. 3, pp. 1349–1359, 1996.
[21] P. Wu, R. Kazys, and T. Stepinski, "Analysis of the numerically implemented angular spectrum approach based on the evaluation of two dimensional acoustic fields. Part I. Errors due to the discrete Fourier transform and discretization," *J. Acoust. Soc. Am.*, vol. 99, no. 3, pp. 1339–1348, 1996.
[22] F. A. Duck, *Physical Properties of Tissue: A Comprehensive Reference Book*. London, UK: Academic, 1990.
[23] S. A. Goss, R. L. Johnston, and F. Dunn, "Comprehensive compilation of empirical ultrasonic properties of mammalian tissues," *J. Acoust. Soc. Am.*, vol. 64, no. 2, pp. 423–457, 1978.

Urvi Vyas received the B.E. degree from Shree Govindram Sekseria Institute of Technology and Science in 2006 and the Ph.D. degree in bioengineering from the University of Utah in 2011.

She is currently a postdoctoral researcher at Stanford University, Palo Alto, CA. Her research interests include MR-guided focused ultrasound surgery, ultrasound imaging, minimally invasive treatments, thermal therapy, and medical devices.

Douglas A. Christensen received the B.S.E.E. degree from Brigham Young University in 1962, the M.S. degree from Stanford University in 1963, and the Ph.D. degree from the University of Utah in 1967. From 1972 to 1974, he held a Special NIH postdoctorate position in biomedical engineering at the University of Washington. He has been a faculty member at the University of Utah since 1971. He currently holds a joint appointment as Professor of Bioengineering and Professor of Electrical and Computer Engineering. His major research interests are in the area of waves in medical diagnosis and therapy, including therapeutic ultrasound, ultrasonic bioinstrumentation, optical biosensors, and numerical modeling of acoustic fields. He is the author of the books *Ultrasonic Bioinstrumentation*, published in 1988, and *Introduction to Biomedical Engineering: Biomechanics and Bioelectricity*, published in 2010, and co-author of *Basic Introduction to Bioelectromagnetics*, 2nd ed., published in 2010.